

Chapter 11

Modelling Tunnel Failure and Fault Re-activation in CO₂ Geo-sequestration



Baotang Shen, Nick Barton, and Jingyu Shi

Abstract Failure of brittle rock is often associated with explicit fracturing events. Understanding fracturing behavior of rock masses has become a critical endeavour for not only civil engineering but also geological radioactive waste disposal, deep mining, geothermal energy extraction and CO₂ geo-sequestration. Numerical simulations are vital tools for this endeavour.

This chapter presents two application cases using FRACOD. The first is generic study on the failure mechanisms of deep tunnels; the second is a true case study using a coupled FRACOD model to investigate the fault stability for a CO₂ geo-sequestration demonstration project in Australia. These application cases will demonstrate that the fracture mechanics based code FRACOD is not only helpful for investigating the rock failure mechanisms but can also be used to assist the design of practical rock engineering operations.

Keywords Deep tunnel · Tensile failure · Shear failure · CO₂ geo-sequestration · Fault activation · FRACOD

B. Shen (✉)

CSIRO Mineral Resources, Brisbane, Queensland, Australia

Shandong University of Science and Technology, Qingdao, China

e-mail: Baotang.Shen@csiro.au

N. Barton

Nick Barton & Associates, Oslo, Norway

e-mail: nickbarton@hotmail.com

J. Shi

CSIRO Mineral Resources, Brisbane, Queensland, Australia

e-mail: jingyu.shi@csiro.au

11.1 Introduction

Rock masses are increasingly employed as the host medium in a vast array of human activities. Facilities like transport tunnels, storage caverns, petroleum wells, and underground power stations are located in a variety of rock types and suffer extra challenges when at significant depth. Excavation stability is imperative for all such constructions, in both the short and long term. The understanding of fracturing of rock masses has become a necessity for deep rock excavations in brittle rocks. Small-scale breakouts around single wells in petroleum engineering help to indicate principal stress direction and the degree of stress anisotropy. Large-scale stress-or-strain induced fracturing in tunnels can lead to massive tunnel failure which not only increases the time and cost of tunnel excavation and maintenance, but also imposes serious safety threats to personnel, and occasionally leads to fatalities.

Failure of brittle rock is often associated with explicit fracturing events. Understanding fracturing behavior of rock masses has become an essential for not only civil engineering but also for geological radioactive waste disposal, deep mining, geothermal energy extraction and CO₂ geo-sequestration. Numerical simulations are vital tools for improved understanding of these complex tasks, and numerous numerical models have been developed (Jing 2003).

However, there are a very limited number of codes that can model fracture initiation and propagation, and the codes that do exist are not designed for application at engineering scales. A unique numerical approach and a computing code, FRACOD, to complex rock failure problems was developed based on fracture mechanics principles and a boundary element method (Shen et al. 2014, also refer to Chap. 5). This code can model rock failure processes caused by explicit fracture initiation, propagation and coalescence both in tensile (mode I) and shear (mode II) mechanisms.

In some engineering applications, such as hydraulic fracturing, fluid flows in the rock fractures must be modelled. The fluid flow alters the pressure on the fracture surfaces, which changes the deformation and effective stresses around the rock fractures. On the other hand, the movement of the fracture surfaces will alter the fluid pressure. Thus hydraulic fracturing (H-F) coupling must be considered in such applications. Chapter 5 outlined a procedure to simulate such coupling for isotropic rock masses.

This chapter presents two applications of FRACOD. The first is a generic study on the fracturing mechanisms of deep tunnels; the second is a true case study using a coupled FRACOD model to investigate the stability of a CO₂ geo-sequestration demonstration project in Australia. These application cases will demonstrate that the fracture mechanics based code FRACOD is not only helpful for investigating the rock failure mechanisms but can also be used to assist in the design of practical rock engineering operations.

11.2 Modelling of Tunnel Failures Using FRACOD

In highly stressed rock (or coal) masses, excavations such as boreholes, tunnels, underground caverns and mining roadways will always create stress redistribution and concentration in the vicinity of the opening. Typically, the radial stress in the roof/wall of the opening will be reduced to near zero whereas the tangential stress will be significantly elevated, and may be several times higher than the in situ stress. In the immediate roof/wall of the opening, uniaxial compressive conditions exist due to the removal of the confining stress. Further away from the roof/wall, however, tri-axial compressive stress condition still exists as the radial stress increases with distance into the rock and acts as the confining stress and thereby increases the rock strength.

The stress redistribution and concentration near the opening often cause rock mass failure in the form of distinct fracturing. Two very different failure modes have been observed, both of them ‘physical realities’ but from very different environments. The first is from petroleum wellbore simulations in sandstones, drilling into polyaxially loaded blocks. With change of scale, a small deep tunnel in a weak but brittle rock can be envisaged. Failure is dominated by (log-spiral) shearing due to the high applied boundary stresses. The second is a real case involving a highly-stressed granite in an underground research laboratory: the Underground Research Laboratory (URL) in Canada. Initiation is by tensile/extensional fracturing, but there is shearing and buckling, and a final characteristic notch is developed on opposite sides of the tunnel.

In many real rock engineering failures, particularly those involving extensive rock burst or coal burst, the fracturing mechanisms are often complex and both tensile and shear fracturing are involved. Figure 11.1 shows two cases of massive failures in highly stressed TBM tunnels. The picture on the left was the aftermath of a

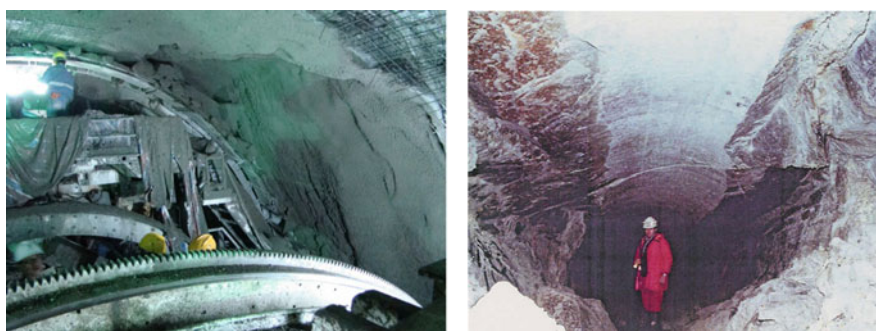


Fig. 11.1 Stress-induced (or extensional-strain induced) fracturing and massive shear failure and rock burst effects in two TBM tunnels. Left – failure in Jinping II Tunnel in marble, China; Right – failure in the earliest UK TBM tunnel of 1880 in chalk marl. (After Barton and Shen 2017)



Fig. 11.2 A coal burst event at Austar Mine, Australia. The coal rib burst out during roadway development. The overburden depth was 550 m. (After NSW Mine Safety Investigation Unit 2015)

minor rock burst in the Jinping II headrace tunnels in China at a depth approaching 1.5 km. In a deeper part of the mountain, many lives were sadly lost in a major rock burst event that destroyed the pilot TBM. The picture on the right was a photo from the UK Channel Tunnel in chalk marl. Massive failure occurred in both cases where shear failure appears to be dominant.

Figure 11.2 shows a coal burst failure occurred at Austar Mine in Australia on April 15, 2014, which resulted in two fatalities. The coal rib of an underground roadway heading suddenly burst out during roadway development. The failed coal is confined vertically by the Dosco Band (a common stone band) within the Greta Seam. The smooth and dominant shear surface presented by the Dosco Band appears to have acted as a dynamic shear failure plane. The mechanisms of the coal failure in the main rib are unclear, but it is highly likely that mixed shear and tensile fracturing have occurred.

This section presents an investigation on failure mechanisms of deep tunnel and underground roadways.

11.2.1 Extensional Strain Criterion for Tunnel Spalling

It has been recognised that both tensile (or extensional strain) initiation and progression in shear have their important roles to play. Tensile initiation may consist of critical strain-initiated extensional fracturing, which can explain several puzzling phenomena such as tensile fracturing in entirely compressive stress fields

(e.g. Fairhurst and Cook 1967). In a recent study, Shen and Barton (2018) used the extensional strain criterion to investigate the tunnel failure mechanisms. This section provides the fundamental details of the extension strain criterion, and its implement into a numerical code: FRACOD, for modelling engineering problems.

Based on the extension strain theory, which was originally developed by Stacey (1981) and later extensively discussed by Wesseloo and Stacey (2016) for its applications, if the strain in a direction becomes tensile and reaches a critical value, tensile fracturing will occur. The original extension strain theory, however, uses the “critical strain” as the measure of failure which is not commonly tested in laboratory, and it does not link explicitly with the known parameters (such as tensile strength σ_t). Here we establish a stress-based formula using the extension strain theory.

A two-dimensional *plane-strain* equation for expressing extensional strain (in the lateral direction) is as follows:

$$\epsilon_3 = (1 - \nu^2)/E [\sigma_3 - \nu\sigma_1] \quad (11.1)$$

where ν is the Poisson’s ratio of the intact rock and E is the Young’s modulus.

From Eq. (11.1), extensional strain may develop in a stress field where both principal stresses are compressive, due to the effect of Poisson’s ratio. This explains why tensile fracturing can occur in the roof/wall of an underground opening where no tensile stress is expected. The only requirement will be that $\nu\sigma_1 > \sigma_3$, i.e. the disparity between the major principal stress (σ_1) and the minor principal stress (σ_3) needs to be high enough.

The critical extensional strain (ϵ_t) for tensile fracturing can be determined using the tensile strength of the rock (σ_t) when a rock specimen is under uniaxial tension ($\sigma_1 = 0$; $\sigma_3 = \sigma_t$), i.e.

$$\epsilon_t = (1 - \nu^2)\sigma_t/E \quad (11.2)$$

Using the critical extensional strain in Eq. (11.2) to replace ϵ_3 in Eq. (11.1) we obtain the critical compressive (i.e. tangential) stress for tensile fracturing (or spalling) to occur:

$$\sigma_1(\text{spalling}) = (\sigma_t + \sigma_3)/\nu \quad (11.3)$$

Considering that the confining stress σ_3 is zero at the wall of an underground opening, then for rocks with typically UCS $\approx 10\sigma_t$ and Poisson’s ratio ≈ 0.25 , tensile fracturing will start when the uniaxial (or tangential) stress reaches $\approx 0.4 \cdot \text{UCS}$. Interestingly many rock engineers, mining engineers and researchers have observed that tunnel spalling starts when the maximum tangential stress (σ_θ) at the tunnel wall reaches around $0.4 \pm 0.1 \cdot \text{UCS}$ (e.g. Martin et al. 1999). Similar phenomon have been found independently by Barton and Grimstad (2014) who reproduced the historic (pre-1990) case records from Grimstad, which show that

ratios of σ_θ/σ_c were mostly in the range 0.4–0.8 for road tunnels of 600–1400 m depth where ‘stress-slabbing’ (extensional strain) and rock burst (shear failures) had occurred. These were the reason for strongly increased SRF in the Q-system tunnel support recommendations, for the case of massive rock (Grimstad and Barton 1993, Barton and Shen 2017).

Extension-strain theory may in fact be the best explanation for field observations of tunnel spalling at lower stress levels, rather than the mobilization of UCS. However, this is at odds with the belief by many that the lower spalling strength was caused by a scale effect on UCS. Many researchers have demonstrated in the laboratory that rock strength can reduce significantly with size (e.g. Hoek and Brown 1980). However, some researchers (e.g. Dresen et al. 2010) found that the borehole spalling stress becomes less size dependent for borehole size greater than 20 mm and the borehole spalling strength converges to a constant. Cai and Kaiser (2014) reviewed many previous laboratory borehole failure (mostly hollow-cylinder) studies and stated that *“although scale-dependent behaviour was observed for smaller holes, the failure hoop stress was almost identical to the uniaxial compressive strength when the hole diameter was greater than 75 mm”*. According to our latest studies, the scale effect on fracture initiation may not be the key mechanism causing the lower spalling strength than UCS for tunnels on the engineering scale. We believe that tunnel spalling is a result of tensile fracturing due to excessive extensional strain caused by the uniaxial/biaxial compression stress state as the tunnel wall is approached.

Tensile fracturing and spalling may be the start of a failure process at the early stage but it is unlikely to be the root cause of massive failure. Further away from the wall/roof of an underground excavation, the confining stress (σ_3) will be higher and the major principal stress will be lower due to the moderation of stress concentration with distance from the opening. Hence, tensile fracturing conditions may not be met anymore. In this region, shear fracturing driven by high shear stress will be dominant.

To demonstrate this effect, Shen and Barton (2018) considered a circular tunnel in a massive rock mass with far-field stresses σ_1 and σ_3 . In the rock mass along the direction of major principal stress σ_1 the tangential and radial stress can be expressed as:

$$\begin{aligned}\sigma_e &= \frac{\sigma_1 + \sigma_3}{2} \left(1 + \frac{a}{r}\right) + \frac{\sigma_1 + \sigma_3}{2} \left(1 + 3\frac{a^2}{r^2}\right) \\ \sigma_r &= \frac{\sigma_1 + \sigma_3}{2} \left(1 - \frac{a}{r}\right) - \frac{\sigma_1 + \sigma_3}{2} \left(1 - \frac{a}{r}\right) \left(1 - 3\frac{a}{r}\right)\end{aligned}\quad (11.4)$$

where σ_θ and σ_r are the tangential stress and radial stress, respectively; a is the tunnel radius; r is the distance to tunnel centre. Below is the process to determine the depth of tensile spalling caused by extensional strain in the tunnel wall and its relationship with the ratio of tangential stress and UCS (σ_{max}/σ_c).

Assuming the far-field stress $\sigma_1 = 2\sigma_3$ and Poisson's ratio $\nu = 0.25$, three cases were examined with different rock compressive strength to tensile strength ratios: $\sigma_c/\sigma_t = 8, 10, 12$. Using Eqs. (11.3) and (11.4), it is possible to obtain the depth of spalling caused by the excessive extensional strain, which is actually the distance (r) where the extensional strain reached the critical value. For any given far-field stress value σ_1 , the spalling distance (r) can be obtained from the solution of Eq. (11.5)

$$3\left(1 + \frac{a}{r}\right) + \left(1 + 3\frac{a^2}{r^2}\right) = \left[\frac{4\sigma_t}{\sigma_1} + 3\left(1 - \frac{a}{r}\right) - \left(1 - \frac{a}{r}\right)\left(1 - 3\frac{a}{r}\right)\right] \frac{1}{\nu} \quad (11.5)$$

Using the relation of $\sigma_{max} = 3\sigma_I - \sigma_3 = 2.5\sigma_I$, Eq. (11.5) can also be expressed in terms of the ratio of maximum hoop stress to rock UCS (σ_{max}/σ_c) and the spalling-depth ratio (R_f/a).

$$\frac{\sigma_{max}}{\sigma_c} = \frac{\frac{1}{10}\left(\frac{\sigma_c}{\sigma_t}\right)}{3\nu\left(1 + \left(\frac{R_f}{a}\right)^{-1}\right) + \nu\left(1 + 3\left(\frac{R_f}{a}\right)^{-1}\right) - 3\left(1 - \left(\frac{R_f}{a}\right)^{-1}\right) + \left(1 - \left(\frac{R_f}{a}\right)^{-1} + \nu\right)\left(1 - 3\left(\frac{R_f}{a}\right)^{-1}\right)} \quad (11.6)$$

Equation (11.6) gives the relationship between the stress ratio (σ_{max}/σ_c) and the spalling depth/radius ratio (R_f/a) for a circular tunnel in an unjointed rock mass with far-field stress $\sigma_1 = 2\sigma_3$. It is obviously dependent on the ratio of rock compressive strength to tensile strength σ_c/σ_t and Poisson's ratio ν . For the commonly used value for brittle rock $\nu = 0.25$ and $\sigma_c/\sigma_t = 10 \pm 2$, Eq. (11.6) gives the critical spalling stress/strength ratio of 0.4 ± 0.08 at the tunnel boundary. This is very close to the empirical value of 0.4 ± 0.1 reported by Martin (1997).

At higher stress ratio (σ_{max}/σ_c), the spalling depth will increase. The spalling ratios (R_f/a) calculated using Eq. (11.6) are plotted against the stress ratio (σ_{max}/σ_c) for the three σ_c/σ_t values in Fig. 11.3, and the curves are compared with the empirical linear envelopes provided by Martin et al. (1999). It can be noticed that for shallow spalling (e.g. $R_f/a \approx 1.0$), Eq. (11.6) gives results similar to the empirical values. However, for extensive tunnel failure (e.g. $R_f/a > 1.2$), the estimated tunnel failure depth using Eq. (11.6) based on the extension strain theory, does not agree with the observed failure depth, and it is much less than the actual observations. This suggests that for deep extensive tunnel failure, the failure mechanism is very different from the tensile fracturing. Note that Eq. (11.6) did not consider the stress redistribution caused by the progressive spalling failure, which could also increase the failure depth from the estimated values. As will be demonstrated by numerical modelling in the next section, shear fracturing instead of tensile fracturing is the dominant failure mechanism for large scale extensive tunnel failure.

Fig. 11.3 Comparison of the estimated tunnel breakout depth using extension strain theory (red solid and dash lines) with the observed results from deep tunnels and mines (black solid and dash lines and black data points). In other words massive shear failures, not tensile failures, are needed to explain the observations at higher stress levels

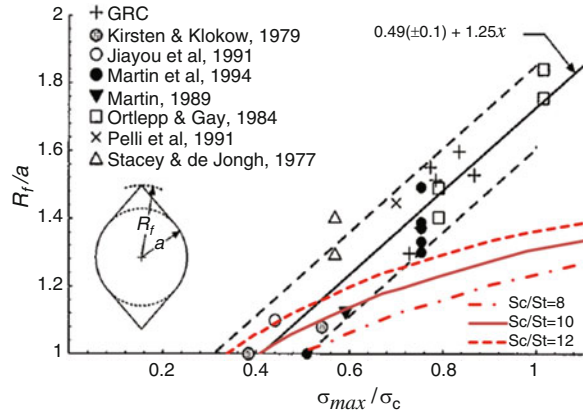
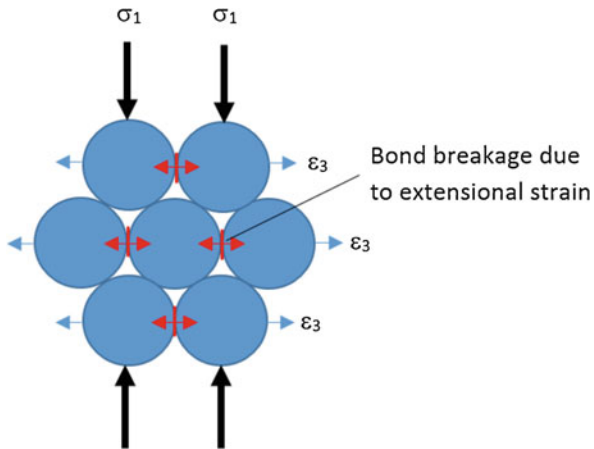


Fig. 11.4 Mechanism of tensile fracturing due to extensional strain caused by compressive loading



The extension strain criterion, although not very new, has not yet been widely used in the rock mechanics community, yet it may hold the key to explain many phenomena such as spalling and sheeting fractures. The core concept of this criterion is that extensional strain could be caused due to compressive loading in the perpendicular direction due to the Poisson’s effect. Physically, this may be understood by the mechanism shown in Fig. 11.4. Considering that the rock is composed of interlocked granular particles, compressive loading (σ_1) in the vertical direction tends to squeeze the particles to move horizontally, forming the “apparent” lateral deformation or extensional strain (ϵ_3). This lateral movement could create tension at the sub-vertical interfaces between the particles. If the loading stress is high enough, the bonds between the particles could break, creating isolated vertical tensile fractures. Note that these vertical tensile fractures may still be confined by the particles

and may only be considered as fracture initiation. At this stage, rock is not yet failed in macroscale and it has not reached its peak strength. Final failure of the rock requires that these isolated tensile fractures coalesce and develop into large failure planes which may involve shear failure of some interfaces between the particles.

The above mechanism can also explain the apparent concern of some researchers that the extension strain criterion could not explain the Uniaxial Compressive Test, namely the rock specimen could fail much earlier than its uniaxial compressive strength if the extensional strain is considered. In fact, when the uniaxial load reaches approximately $0.4 \cdot \text{UCS}$, only isolated tensile fractures start to develop in the rock specimen due to the lateral extensional strain, as shown in Fig. 11.4. This coincides with the so-called “fracture initiation” stage observed in the laboratory by many researchers, and with the commencement of Acoustic Emission (AE) events. However, these tensile fractures are short and not interlinked in the rock specimen, and therefore are not yet able to cause the rock specimen to fail. Final failure of the specimen will be formed by coalescence of the fractures at a much higher load.

11.2.2 Modelling Extensive Failure in Deep Tunnels

FRACOD has been used recently to simulate several generic cases for deep tunnels (Shen and Barton 2018). A number of FRACOD models have been used to investigate the mechanisms of tunnel spalling/failure. In all cases, an 8 m diameter tunnel was assumed to be excavated, first of all in an elastic and massive rock mass *without joints*. The *in situ* stress state in the plane of the tunnel cross-section was assumed to be represented by a stress ratio of $\sigma_{\text{Hmax}}/\sigma_{\text{v}} = 2.0$ and a simulated depth of 1000 m were modelled in the tests.

11.2.2.1 Model Without Joints

The input parameters in this model are given as follows. Boundary stresses: $\sigma_{\text{Hmax}} = 50$ MPa; $\sigma_{\text{v}} = 25$ MPa. For the base case, the strength and fracture toughness of the rock are: UCS = 165 MPa; cohesion $c = 31$ MPa; internal friction angle $\phi = 49^\circ$; tensile strength $\sigma_{\text{t}} = 14.8$ MPa; mode I fracture toughness $K_{\text{IC}} = 3.8$ MPa m^{1/2} and mode II fracture toughness $K_{\text{IIC}} = 4.7$ MPa m^{1/2}.

These parameters are the same as those of Äspö diorite, and are listed in the literature (e.g. Siren 2012 who compares Finnish and Swedish rocks). The maximum tangential stress at the tunnel was calculated to be $\sigma_{\text{max}} = 125$ MPa, and the ratio of $\sigma_{\text{max}}/\text{UCS} = 0.75$. Based on Martin et al. (1999), the ratio of expected failure depth to tunnel radius is $R_{\text{f}}/a = 1.3\text{--}1.5$.

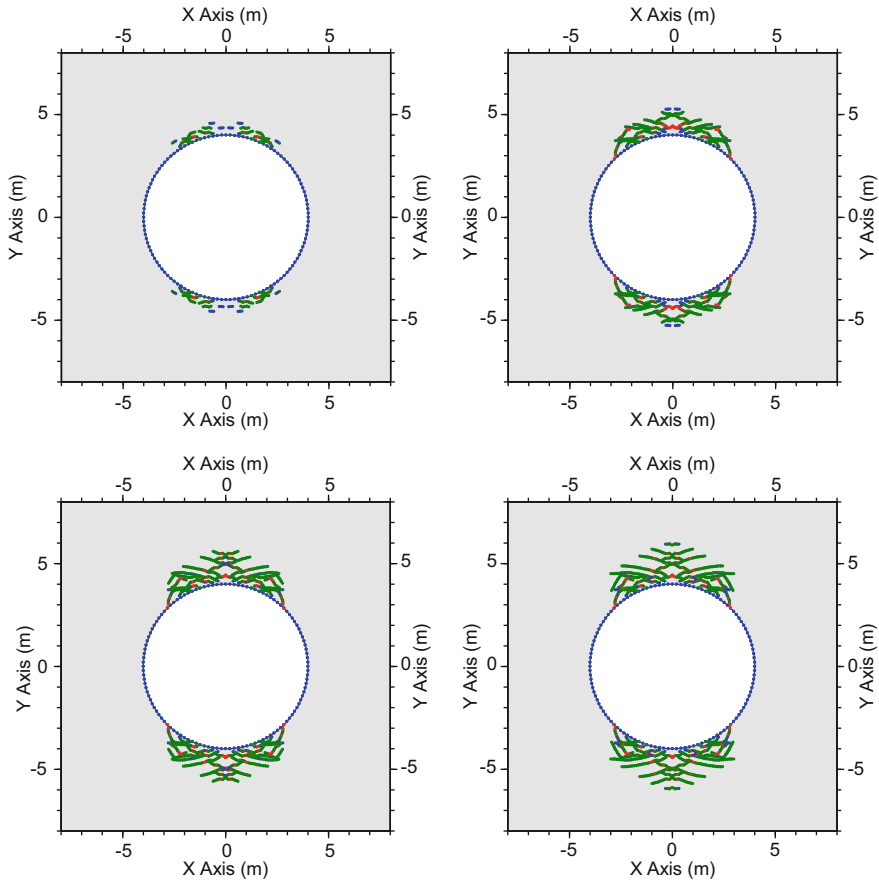


Fig. 11.5 A FRACOD model of a 1 km deep tunnel, showing some of the progressive stages of fracturing, first due to extensional-strain induced failure in tension (in red) despite the compressive stress field, followed by log-spiral style (and connecting) larger-scale shearing (in green)

For the above case, the predicted failure process using FRACOD is shown in progression in Fig. 11.5. The key observations are:

1. Fracture initiation occurred in the roof and floor where the compressive stress was the highest. The fracture initiation was driven by tensile strain due to the high compressive stress, and the initiated fractures were sub-parallel to the surface of the tunnel wall.
2. Fractures were not expected to propagate in tension because there is no tensile stress in the vicinity of the tunnel. In fact, FRACOD predicts that they propagate in shear, forming a kink path from the initial fractures and they continue to propagate at an angle from the tunnel surface.

3. As the propagation of the fractures near the tunnel surface progresses, new fractures continue to form deeper into the rock. These fractures also propagate in shear, eventually forming a larger (potential) breakout.
4. The ratio of failure depth to tunnel radius (R_f/a) is predicted to be 1.5, which is close to the upper limit predicted by Martin et al. (1999).

Overall for this generic case, the modelling results indicate that the fractures initiate due to extensional–strain related failure-in-tension mechanisms. However, the overall formation of the tunnel failure is predominately caused by shearing, since stress levels are sufficiently high.

11.2.2.2 Model with Joints

Several models with joint sets were then modelled. These models had the same rock mechanics properties as those shown in Fig. 11.5. The joint mechanical properties are assumed to be: normal stiffness $K_n = 2000$ GPa/m; shear stiffness $K_s = 200$ GPa/m; friction angle = 30°; dilation angle = 2°; initial cohesion = 31 MPa. The predicted fracturing patterns in the vicinity of the tunnel for three jointed models are shown in Fig. 11.6. The introduction of joints in the model has led to less fracturing in the tunnel roof and floor, due presumably to the stress releasing effect of the jointing. The fracturing pattern is significantly affected by the joint geometry. The existence of joints did not change the overall fracturing mechanisms of the tunnel breakout, i.e. a mixed tensile and shear failure, with shear failure being the dominating cause. However the extent of the fracturing through intact rock (the actual need for fracturing) was obviously much reduced, as shear stresses could be dissipated to some extent by movement along the joints. Rougher joints would be expected to have subtle effects, probably in the direction of more extensional and shear fracturing, as dilation would tend to reduce shearing along the joints, and reduce shear stress dissipation.

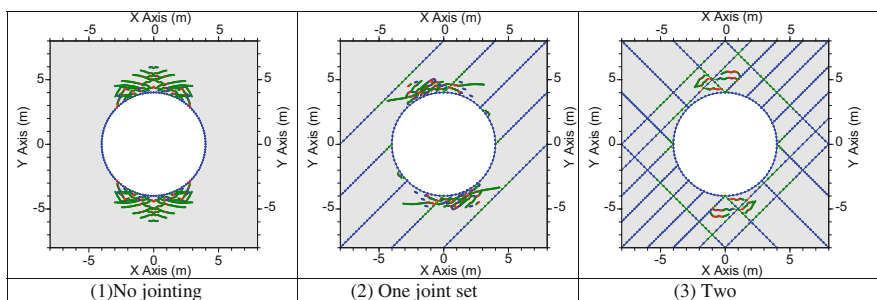


Fig. 11.6 A comparison of fracturing behaviour when intact rock is replaced by a model with one and then by two sets of inclined jointing. Shearing along the joints is evident, and hence the much reduced fracturing of intact rock, especially when the joints are more closely spaced

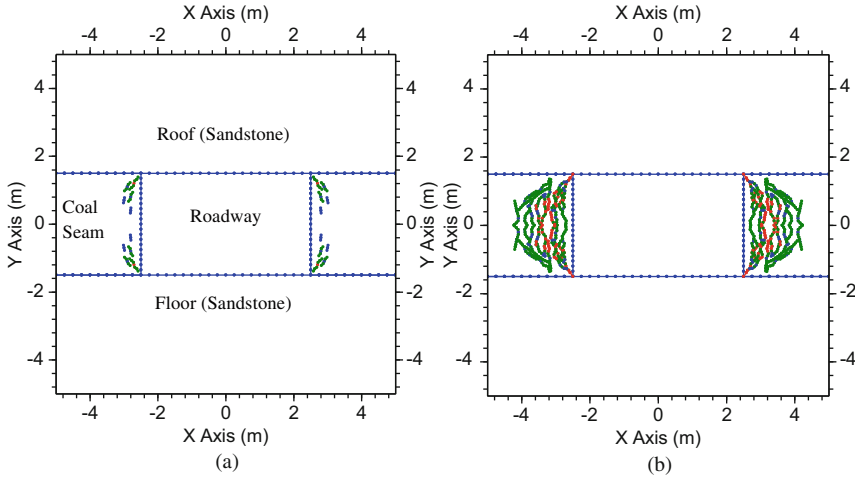


Fig. 11.7 Predicted failure in roadway ribs due to fracture initiation and propagation. (a) Early stage of fracturing; (b) final stage of failure

11.2.3 Modelling Extensive Roadway Failure in Underground Coal Mines

Several models have been used to simulate the rib failure around a roadway heading, in an underground coal mine. The roadway has a rectangular shape with a size of 5 m (width) and 3 m (height). The coal seam has a thickness of 3 m, and it is assumed to be overlain and underlain by massive sandstone units. The roadway is at a depth of 500 m with *in situ* stresses $\sigma_{Hmax} = \sigma_v = 12.5$ MPa. The strength and fracture toughness of the rock and coal are: Coal: UCS = 10 MPa; cohesion $c = 2.3$ MPa; internal friction angle $\phi = 41^\circ$; tensile strength $\sigma_t = 0.1$ MPa; *mode I* fracture toughness $K_{IC} = 0.1$ MPa m^{1/2} and *mode II* fracture toughness $K_{IIC} = 0.3$ MPa m^{1/2}, Young's modulus $E = 2.0$ GPa, and Poisson's ratio = 0.25. Sandstone: UCS = 80 MPa; Young's modulus $E = 20$ GPa, and Poisson's ratio = 0.25. Fracturing is considered only in the coal seam. No failure is assumed in the much stronger sandstone units. These data are based on a real underground mine case in Australia.

The first model was run without considering explicitly the cleats or joints in the coal seam. After the roadway excavation, fracture initiations occur in the coal rib near the roof and floor corners where the stress concentration is severe, and short fractures parallel or at a small angle with the rib wall are formed (see Fig. 11.7). These short fractures are caused by tensile strain resulting from the high compressive stress. The fractures however tend to propagate in shear and coalesce with each other to form larger fractures. The fracture initiation and propagation develops progressively deeper into the roadway ribs. Finally, a large failure zone in the coal rib is formed where the coal is extensively fractured. The depth of the failure zone is about 1.7 m.

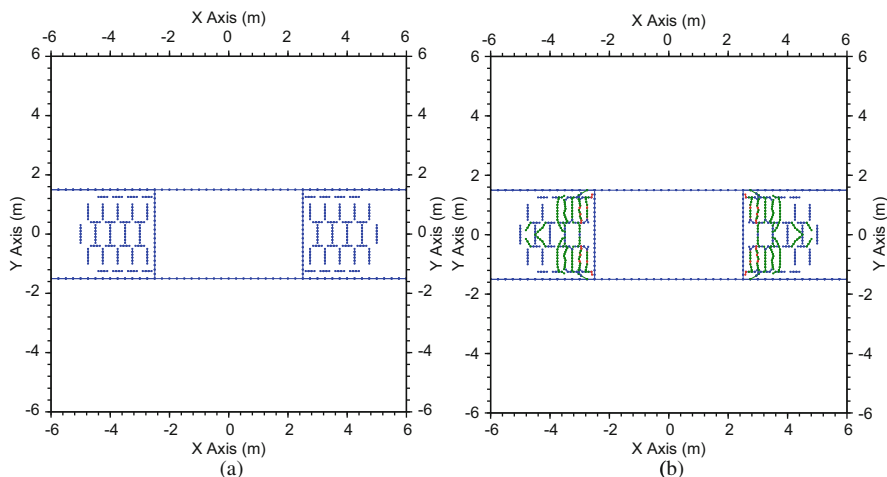


Fig. 11.8 Predicted failure in roadway ribs when short joints (cleats) are considered. **(a)** Initial status with joint system; **(b)** final stage of the failure. Note that the boundaries are for plot only. The model is assumed to be in an infinitely large rock mass

It is noticed that the fracture propagation in the failure region is dominated by shearing although fracture initiation is mainly due to tensile strain and limited tensile fracture propagation are also involved in the process. Shear fractures are likely to be unstable which could release strain energy very rapidly and cause the coal seam to burst, as experienced.

The second model considers two sets of short joints (cleats) in the seam, one in the vertical direction and the other in the horizontal direction (Fig. 11.8). The joints have a limited length and are contained in the coal mass. The joint mechanical properties are assumed to be: normal stiffness $K_n = 10$ GPa/m; shear stiffness $K_s = 10$ GPa/m; friction angle = 30° ; dilation angle = 0° ; cohesion = 0 MPa. All other geometrical and mechanical parameters are the same as in the first model (Fig. 11.7). The predicted failure in the ribs starts near the upper and lower corners mainly caused by the propagation and coalescence of the existing short joints. The failure then expands deeper into the rib and toward the mid-height of the rib, eventually forming a failure zone of about 1.2 m width in the rib. Some limited fracture propagations also occur further into the rib, but they do not appear to form any major failure.

It was observed that fractures occurred in the first 0.5 m from the roadway walls, and they were caused by mixed tensile and shear failures. However, deeper than 0.5 m into the rib the fracturing was mostly caused by shearing. Shear fracturing is often unstable and it releases excessive strain energy. This may indicate that dynamic failure could occur in such highly-stressed roadway ribs.

Consistent with previous tunnel cases, the modelling results also indicate that pre-existing joints or cleats in the coal seam have reduced the intensity and the extents of rock fracturing. Compared with the case without joints (Fig. 11.7), the

model with joints has less fracturing in the rib and the range of rib failure is reduced from 1.7 m to about 1.2 m. Pre-existing joints or cleats can desorb some strain energy through joint deformation and sliding, and hence can apparently reduce the severity of an otherwise violent failure.

11.3 Modelling CO₂ Geo-sequestration – An Experiment Using FRACOD

Geological storage of carbon dioxide (CO₂) has been proposed as a potential method of reducing greenhouse gas emissions. The Naylor Field in the Otway Basin, Victoria, Australia has been chosen as a demonstration site (The Otway Project) for the geological storage of CO₂ by the Cooperative Research Centre for Greenhouse Gas Technologies (CO₂CRC) (Cook 2014). The Naylor Field is a small depleted natural gas field, with the original gas cap area estimated at 40 ha that originally held a methane-rich gas accumulation. This resource was exhausted before injection of CO₂. The field is a fault-bound gas trap (Fig. 11.9) (Vidal-Gilbert et al. 2010). The Naylor Field is bound to the west by a north-south trending normal fault (Naylor Fault in Fig. 11.9). The Naylor Fault has an effective juxtaposition seal since the fault throw is insufficient to completely offset the seal (Belfast mudstone). The Naylor Fault forms part of the structural closure which contains the injected CO₂ plume and is required to act as a long-term seal. The Naylor structure is

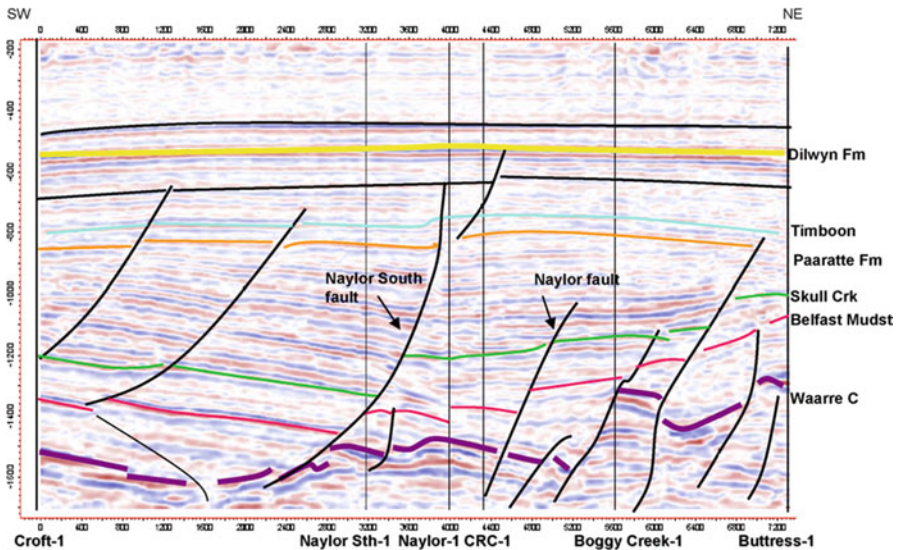


Fig. 11.9 Major faults identified by the 3D seismic reflection survey and drilling of four wells. (After Vidal-Gilbert et al. 2010)

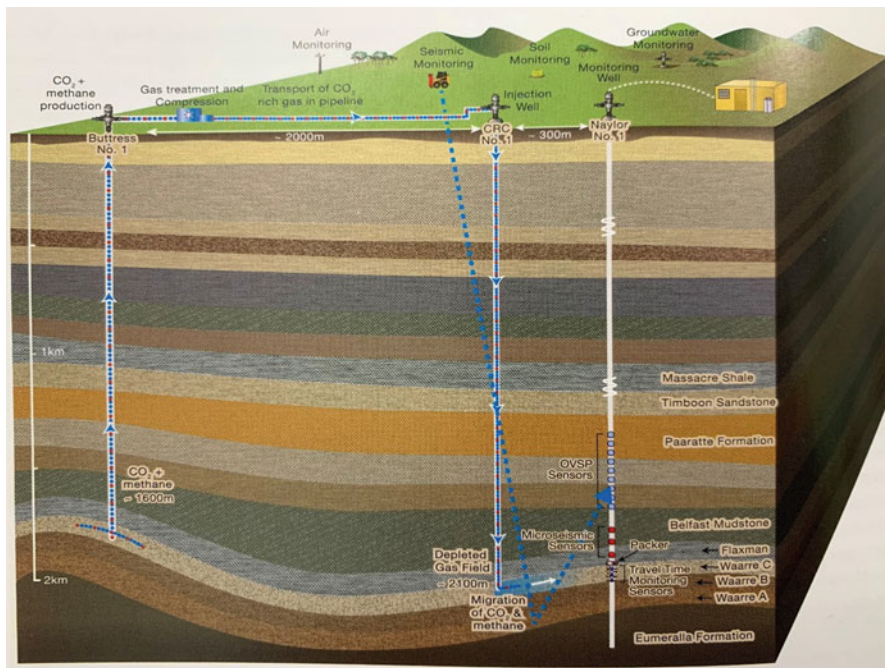


Fig. 11.10 Geological setting in the CO₂CRC Otway Project area. (After Cook 2014)

also cut to the east by a normal fault (Naylor East Fault) and it is bound to the South by the Naylor South Fault (Fig. 11.9). Neither the Naylor East Fault nor the Naylor South Fault is in the expected migration pathway of the injected CO₂ plume. The faults bounding the Naylor field supported the initial natural gas column, and the injected volume of CO₂ at subsurface conditions was smaller than the volume of produced methane under the same conditions. Therefore, the faults bounding the Naylor Field should have sufficient sealing capacity to hold the CO₂ volume injected.

The target horizon for CO₂ injection is the Late Cretaceous Waarre Formation (Waarre C in Fig. 11.10). The Waarre Formation is overlain by the Flaxmans Formation and the Belfast mudstone. This site was selected as the location for a CO₂ injection pilot project due to the good porosity and permeability of its reservoir rock (the average permeability was more than 1 Darcy). Furthermore, the reservoir is overlain by the laterally extensive and thick Belfast mudstone, which, based on laboratory analyses, should be able to support a CO₂ column height in the range of 607–851 m with an average of 754 m (Daniel 2007).

There are three wells in the Naylor Field: Naylor-1 being the up dip monitoring well, Naylor South-1 (not shown in Fig. 11.10) and CRC-1 used as the CO₂ injection wells. CO₂-rich gas has been produced from a nearby field and injected into the CRC-1 borehole within the Naylor Structure to demonstrate the viability of geological sequestration of CO₂ in Australia. The reservoir was monitored before, during

and after injection via down hole pressure and temperature gauges in the injection well, fluid sampling from the reservoir at the Naylor-1 observation well (via a three level U-tube assembly), and various geophysical methods including 3D seismic and microseismic equipment.

The orientation of maximum horizontal stress was determined to be $N142 \pm 5^\circ E$ and is approximately parallel to the strike direction of Naylor fault and Naylor South fault. The magnitudes of the maximum and minimum horizontal stresses have been estimated by various means (Vidal-Gilbert et al. 2010):

$$\sigma_{Hmax} = 18.5 \times Z \text{ (MPa)}, \sigma_{hmin} = 14.5 \times Z \text{ (MPa)}, \sigma_v = 21.45 \times Z \text{ (MPa)}$$

where σ_{Hmax} is the maximum horizontal stress, σ_{hmin} is the minimum horizontal stress, σ_v is the vertical stress and Z is depth in km.

A case study applying FRACOD to the Otway Project has been conducted by Shen and Shi (2016). Using the FRACOD code, a two-dimensional numerical model for the injection area is created. The model plane is taken as a vertical cross section in the direction of the minimum horizontal principal stress ($N48^\circ E$) as shown in Fig. 11.11. The Naylor fault and Naylor South fault are assumed to be planar for

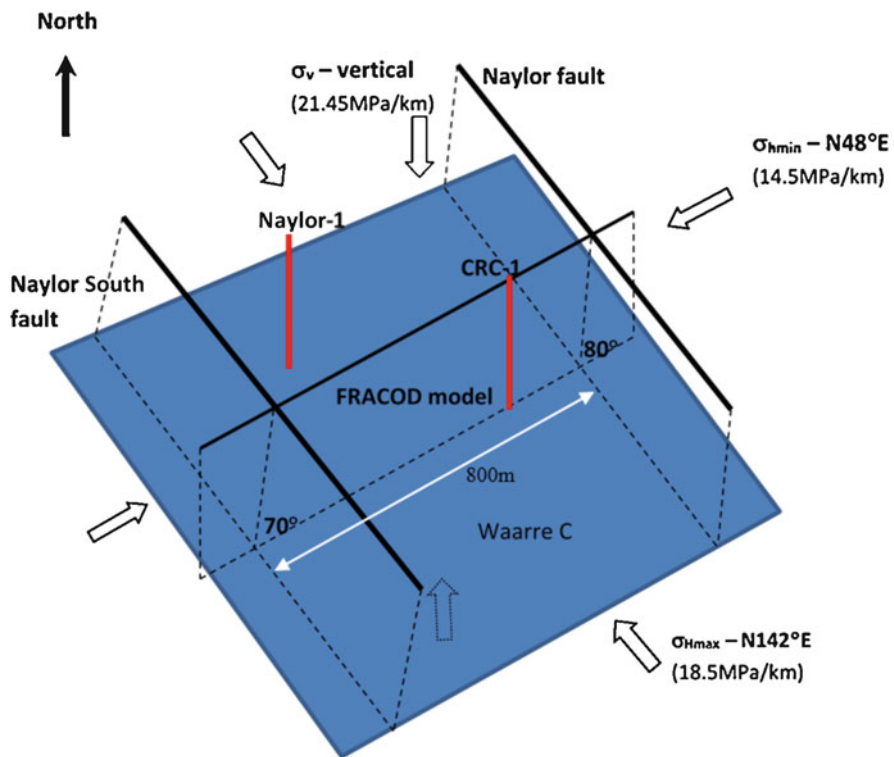


Fig. 11.11 Geometric relationship of faults planes, wellbores, FRACOD model and *in situ* stresses of the Otway Project for CO₂ geo-sequestration

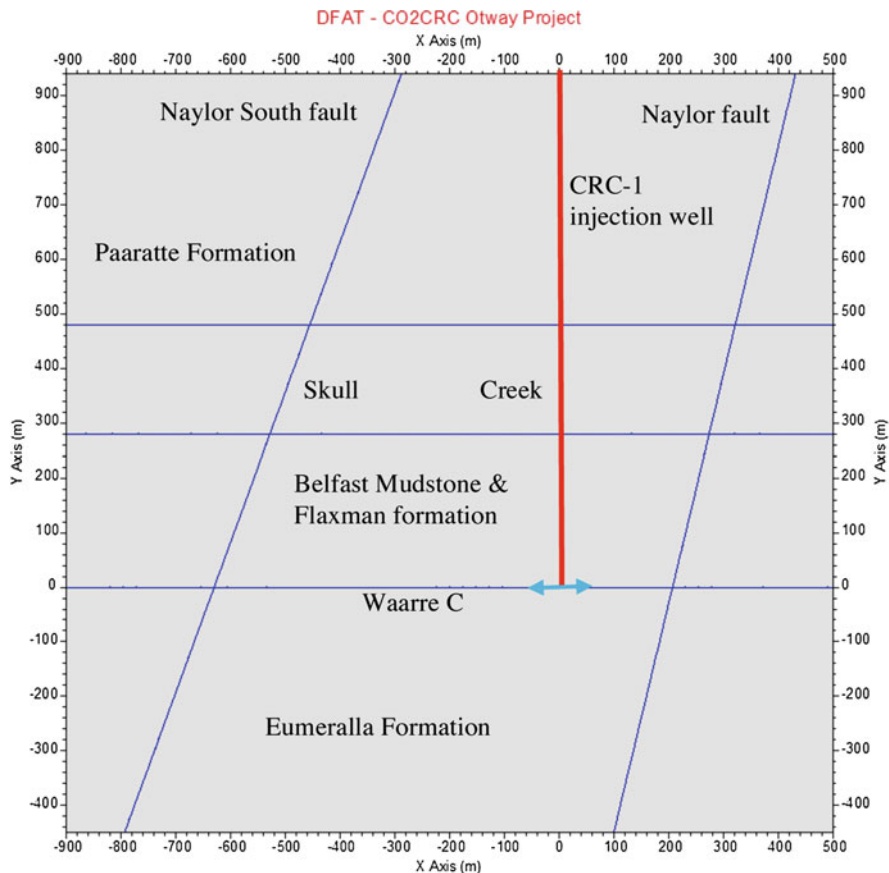


Fig. 11.12 FRACOD model with simplified geology

simplicity and as they are approximately perpendicular to the model cross section they can be well represented in the FRACOD model. With this model, σ_{hmax} is in a direction perpendicular to the model plane and thus only σ_{hmin} and σ_v effect the computation. The two faults are dipping 70° and 80° to the SW respectively. The injection well, CRC-1, is located along the y-axis of the coordinate system, as shown in Fig. 11.12 for the case of a simplified model.

The Waarre C reservoir formation is a permeable layer with thickness of about 35 m. It is relatively thin at the model scale, so this layer is simplified as a fracture with a preset hydraulic aperture that results in the same hydraulic conductivity as a permeable layer. Due to this simplification, the modelling flow time will be significantly different from the actual flow time. Hence, this study will only investigate the quasi-static processes of the fracture fluid flow and mechanical response of the cap rock and the faults. No attempt is made to study the fully dynamic fluid processes. The strength of the existing faults is critically important for investigation of the

possibility of fault re-activation during CO₂ injection. Friction angle of 31° and cohesion of 0.001 MPa used by Aruffo et al. (2014) for the faults at Otway project site are employed here for both the Naylor fault and the Naylor South fault.

The cap rock within a distance of 500 m above the reservoir consists of several different rock formations including Belfast Mudstone, Flaxman formation, Skull Creek Formation and Paaratte Formation. For consideration of stability of the sequestration structure, only the immediate overlaying rock formation (i.e. the Belfast Mudstone and Flaxman formation) is likely to be affected significantly by CO₂ injection. Therefore, uniform rock mass mechanical properties representing those of Belfast Mudstone & Flaxman formation are assumed for the whole model. The rock mass is assumed to be transversely isotropic with parameter values used by Aruffo et al. (2014) and estimated with the experimental data of shale by Islam and Skalle (2013). Key input parameters used in this simulation are listed in Table 11.1 and it should be noted that the CO₂ under the conditions in the reservoir is at liquefied or near liquefied state.

At the time of injection starting for the demonstration project, the reservoir pressure was 16 MPa. This pressure together with its hydraulic gradients is taken as the initial pore pressure in the fractures and faults in the model. For sensitivity studies, however, a case with zero initial pore pressure has also been investigated. During the actual injection the reservoir pressure increased from the initial pressure of 16 MPa to about 19.2 MPa at the end of the injection. A fluid pressure boundary condition is used for the fracture (Waarre C) element at the injection well to simulate the injection process. The difference between the injection pressure and the reservoir pressure will drive the fluid flowing into neighbouring elements in the Waarre C formation and later into the Naylor and Naylor South faults. We consider two stability issues for the CO₂ geo-sequestration project: fault reactivation and cap rock fracturing.

11.3.1 Fault Re-activation

The stability of the faults is related to the fluid pressure in the faults. Increasing the fluid pressure reduces the effective normal stress and can lead to shear failure of a fault. Fault shearing could be associated with dilation of the material in the fault (unless it is dominated by clay cores) and hence the increase of hydraulic aperture of the fault. If the fluid pressure is higher than the *in situ* normal compressive stress, faults will open and this will dramatically increase their hydraulic conductivity. In both cases, the faults could become the path of CO₂ flow into the upper rock formation, and cause leakage of the injected CO₂ toward the surface.

Actual injection pressure at the site was 19.2 MPa with initial pore pressure of 16.0 MPa. In order to investigate possibility of re-activation of the faults, a number of fluid injection pressures from 19.2 MPa to 30 MPa have been considered in FRACOD simulation. In addition, initial pore pressure and fault aperture have been varied to study their sensitivities on the fault re-activation. The values of these parameters and the corresponding modelling results are shown in Table 11.2.

Table 11.1 Input parameters for modelling Otway CO₂ geo-sequestration project

Parameter	Value used
<i>Rock mechanical parameters</i>	
Young's modulus, E_x (GPa) (in horizontal plane)	6.58
Young's modulus, E_y (GPa) (in vertical direction)	16.07
Poisson's ratio, ν_{xz} (in horizontal plane)	0.21
Poisson's ratio, ν_{yx} (in vertical plane)	0.30
Shear modulus, G_{xy} (GPa)	4.5
Uniaxial compressive strength, UCS (MPa) (horizontal & vertical)	14.83
Tensile strength, σ_t (MPa) (horizontal & vertical)	4.44
Internal friction angle ($^\circ$) (horizontal & vertical)	28.1
Fracture toughness Mode I, K_{IC} (MPa/m ^{1/2}) (horizontal & vertical)	0.75
Fracture toughness Mode II, K_{IIC} (MPa/m ^{1/2}) (horizontal & vertical)	1.5
Density, ρ (kg/m ³)	2186
Acceleration of gravity, g (m/s ²)	9.81
Reservoir depth, (m)	2010
<i>Fracture parameters</i>	
Normal stiffness, K_n (GPa/m) (Waarre C)	0.345
Shear stiffness, K_s (GPa/m) (Waarre C)	0.345
Fracture aperture a (m) (Waarre C)	7.29×10^{-3}
Dilatation angle, ψ (deg) (Waarre C)	0
Fracture cohesion, c (MPa) (Waarre C)	5
Friction angle, ϕ (deg) (Waarre C)	37.2
Normal stiffness, K_n (GPa/m) (Naylor and Naylor South fault)	40
Shear stiffness, K_s (GPa/m) (Naylor and Naylor South fault)	15
Fracture aperture a (m) (Naylor and Naylor South fault)	0.1×10^{-3}
Dilatation angle, ψ (deg) (Naylor and Naylor South fault)	1
Fracture cohesion, c (MPa) (Naylor and Naylor South fault)	0.001
Friction angle, ϕ (deg) (Naylor and Naylor South fault)	31
<i>Hydraulic fracture parameters</i>	
Fluid density, ρ_w (kg/m ³)	773
Dynamic viscosity of the fluid, μ (Pa•s)	0.09922×10^{-3}
Initial pore pressure P_0 (MPa)	16
Fluid bulk modulus E_w (MPa) ^a	20
Equivalent hydraulic aperture for Waarre C formation (m)	7.29×10^{-3}
Cap rock hydraulic conductivity (m/s)	1.0×10^{-19}

^aLow fluid bulk modulus is used for faster fluid modelling convergence and better model stability

Overall, with an injection pressure of 19.2 MPa, neither the Naylor South nor the Naylor fault is predicted to show any shear or opening failure regardless of the magnitude of fault aperture and/or existence of a controlled pore pressure. This is consistent with other study results obtained by Aruffo et al. (2014) and Vidal-Gilbert et al. (2010) and the actual injection experiment data. Therefore, under the assumptions used in the modelling, the injection pressure of CO₂ at Otway site is considered to be appropriate and unlikely to cause fault re-activation.

Table 11.2 Summary of modelling results on fault re-activation

Injection pressure (MPa)	Pore pressure = 0		Pore pressure = 16 MPa	
	Fault aperture = 0.1 mm	Fault aperture = 1 mm	Fault aperture = 0.1 mm	Fault aperture = 1 mm
19.2	No fault shearing or opening	No fault shearing or opening	No fault shearing or opening	No fault shearing or opening
25	Very limited fault shearing at Naylor South fault below Waarre C	Major fault shearing at Naylor South above Waarre C	Very limited fault shearing at both faults near Waarre C	Major fault shearing at both faults above and below Waarre C.
	No fault opening	No fault opening	No fault opening	Fault opening near Waarre C
30	Very limited fault shearing or opening near Waarre C	Major fault shearing at both faults above and below Waarre C	Major fault shearing at both faults above and below Waarre C	Major fault shearing at both faults above and below Waarre C
		No fault opening	Limited fault opening.	Limited fault opening.

If there is no pore pressure and the faults are relatively impermeable (aperture = 0.1 mm), then when the injection pressure is increased to 25 MPa, very limited shear failure is predicted to occur in the Naylor South fault above Waarre C, but not in Naylor fault and Naylor South fault below Waarre C. If the faults have a high permeability (aperture = 1 mm), both Naylor South and Naylor faults are predicted to experience some shear failure. The shear failure has a large extension above Waarre C in the Naylor South fault. At this level of injection pressure and no pore pressure, the faults remain closed. When the injection pressure reaches 30 MPa, both the faults are predicted to experience shear failures within a limited distance from Waarre C for a relatively low fault permeability assumption and over an extensive region for a high fault permeability.

The presence of initial pore pressure in the Waarre C reservoir and the two sub-vertical faults accelerates the injected fluid pressure propagation in the reservoir and further into the faults. In this study, the pore pressures in the reservoir and faults are assumed to be the same. Modelling results tabulated in Table 11.2 indicate that with pore pressure of 16 MPa, the extent of fault shearing and opening is greater than those cases of initially zero pore pressure for injection pressure of 25 MPa and 30 MPa.

The model was run for 100 cycles for each combination of injection pressure, pore pressure and fault permeability. It was found that 100 cycles was sufficient for the fluid pressure (in the Waarre C reservoir) to propagate well beyond the Naylor fault and Naylor South fault. Note that each cycle includes one mechanical step (fracture movement and/or propagation) and 50,000 fluid flow calculation steps. In these simulations we did not attempt to replicate the real flow time as discussed previously. Hence the faults are under full injection pressure, at least at their intersections with the Waarre C formation.

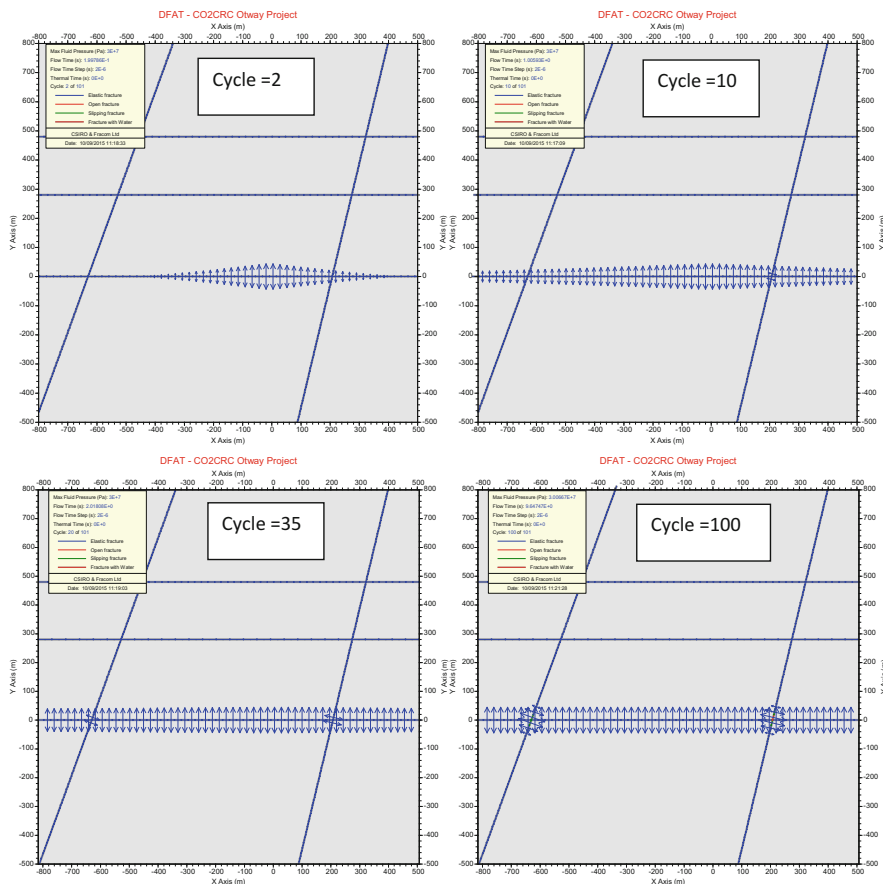


Fig. 11.13 Modelled fluid pressure distribution and the resultant fault shearing and opening. Initial pore pressure = 0 MPa, injection pressure = 30 MPa, fault hydraulic aperture = 0.1 mm. Green indicates fracture shearing and red for fracture opening

Depending on the aperture (permeability) of the fault, the fluid pressure may be able to penetrate into the fault causing large scale fault shearing. One typical case of the fluid pressure distribution and fault shearing is shown in Fig. 11.13 where the initial pore pressure is assumed to be zero and the injection pressure is 30 MPa. At the early stage of the injection, modelling predicts that the injected CO₂ quickly spreads in the Waarre C formation (fracture). After about 35 cycles, fluid starts to penetrate into the Naylor fault and Naylor South fault. The Naylor South fault is the first one to start having limited shearing at the intersection due to its more favourable dip angle (70°). Then the Naylor fault also experiences limited shearing. Shearing however is predicted to be limited only to a distance of several tens of metres above and below the Waarre C formation. This is because the faults have a low permeability (hydraulic aperture = 0.1 mm) and the injected fluid can only penetrate a short

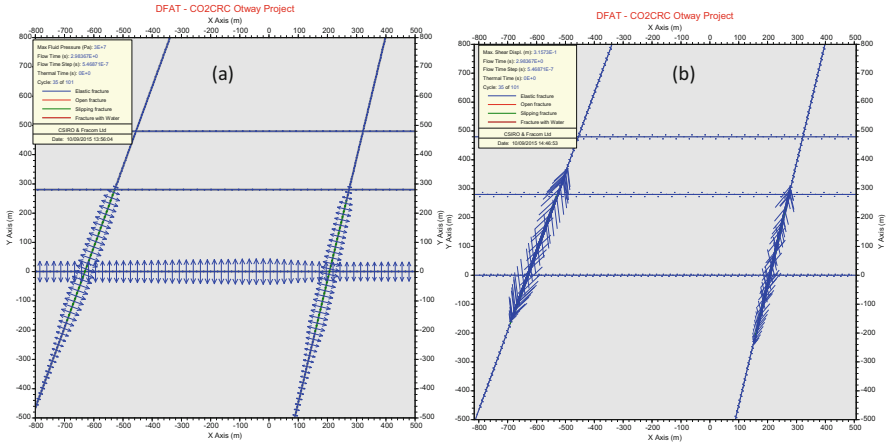


Fig. 11.14 Modelled fluid pressure distribution and the resultant fault shearing at 35 cycles. Initial pore pressure = 0 MPa, injection pressure = 30 MPa, fault hydraulic aperture = 1 mm. (a) Fluid pressure; (b) Fracture shear displacement

distance. This fault is almost vertical (dip = 80°), therefore when the fluid pressure in the fault is close to the minimum horizontal stress ($\sigma_{hmin} = 30.45$ MPa at the depth of Waarre C formation), it may open in tension. Close to the end of the simulation, the part of the Naylor fault at the intersection with Waarre C is predicted to fail in tension, see Fig. 11.13.

A case where the injected CO₂ penetrates into the faults and causes major fault shearing is shown in Fig. 11.14. In this simulation the hydraulic aperture of both faults is set to be 1 mm. As the hydraulic conductivity is proportional to the cube of the fracture hydraulic apertures based on the Cubic Law, the actual hydraulic conductivity has increased to 1000 times from the value used in Fig. 11.13. Due to the significantly higher fault hydraulic conductivity, it is predicted that the injected CO₂ penetrates into the faults at an early stage, and eventually results in a significant length of the faults being re-activated by shearing.

It needs to be mentioned that this study uses the most likely mechanical parameters available from previous studies with a limited parametric sensitivity study. Fault re-activation is a topic with great significance not only for CO₂ geo-sequestration but also for geothermal, nuclear waste disposal etc., and it is being intensively researched and debated. The mechanisms of fault re-activation are very complex, and many factors affect the fault re-activation, such as geology, fault geometry, filling, fluid, thermal gradient, etc. This study is designed to study one aspect of fault reactivation, namely using fracture propagation principles to understand effect of fluid injection on the fault shearing or opening. It was not the purpose of this study to exhaust all the possibilities by doing a very extensive sensitivity study.

11.3.2 Cap-Rock Stability

Injection of pressurised CO₂ into the Waarre C reservoir will increase local fluid pressure and hence will change the effective stress in the reservoir. This will cause a change in the stress field of the surrounding rock mass, including the cap-rock. It is noticed that an injection pressure of 19.2 MPa into a reservoir with pore pressure of 16 MPa does not necessarily mean that it will apply an additional 3.2 MPa vertical stress to the cap-rock. This is because the total vertical stress in the cap-rock is from overall deformation caused by the overburden gravity force, *in situ* stresses and the injection pressure. A change of the fluid pressure in the reservoir will cause uneven deformation of the Waarre C layer and may lead to an increase of vertical stress in some areas and a decrease in other areas.

Depending on the magnitude of injection pressure, the actual increase in vertical stress in the cap-rock immediately above the Waarre C reservoir is predicted to be less than 0.17 MPa, 0.35 MPa and 0.54 MPa respectively for injection pressures of 19.2 MPa, 25 MPa, and 30 MPa. This maximum vertical stress change occurs only in the early stage of the injection and near the injection well, as seen in Fig. 11.15 which shows the predicted change of vertical stress in the cap-rock immediately above the Waarre C reservoir for injection pressure of 30 MPa. During the initial stages of injection, the high fluid pressure is only distributed in the vicinity of the

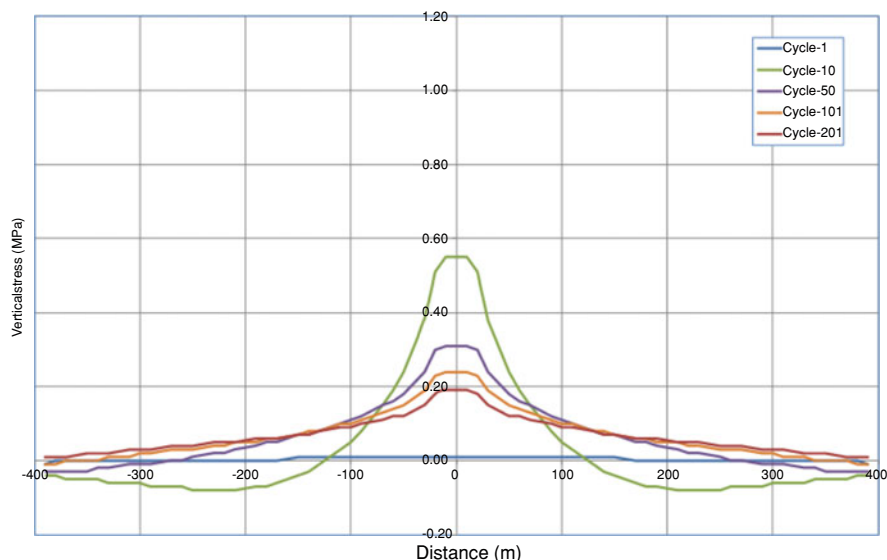


Fig. 11.15 Predicted change of vertical stress in the cap-rock immediately above the Waarre C reservoir. Initial pore pressure = 16 MPa; injection pressure = 30 MPa. Note the distribution of the stress change with flow process after different modelling cycles

injection well and has not yet spread into a wide area of the reservoir. At later stages of injection when the fluid pressure is spread more evenly into the reservoir, the induced vertical stress change gradually diminishes.

Comparing with the magnitude of the *in situ* vertical stress at the Waarre C depth (43.1 MPa) and the uniaxial compressive strength of the cap-rock (14.8 MPa), a change of vertical stress of less than 0.5 MPa due to CO₂ injection is insignificant. It is therefore not expected that the injection pressure up to 30 MPa would cause intact rock failure and compromise the integrity of the cap-rock.

The above findings are for intact rocks. However the cap-rock may contain discontinuities such as joints and weak bedding planes and the strength of the cap-rock could be dominated by the strength of these discontinuities rather than that of intact rock. To investigate the possibility of cap-rock failure due to discontinuities, a case with a pre-existing joint near the injection well has been modelled, see Fig. 11.16. Three joint dip angles (45°, 60° and 90°) are simulated. The joint has

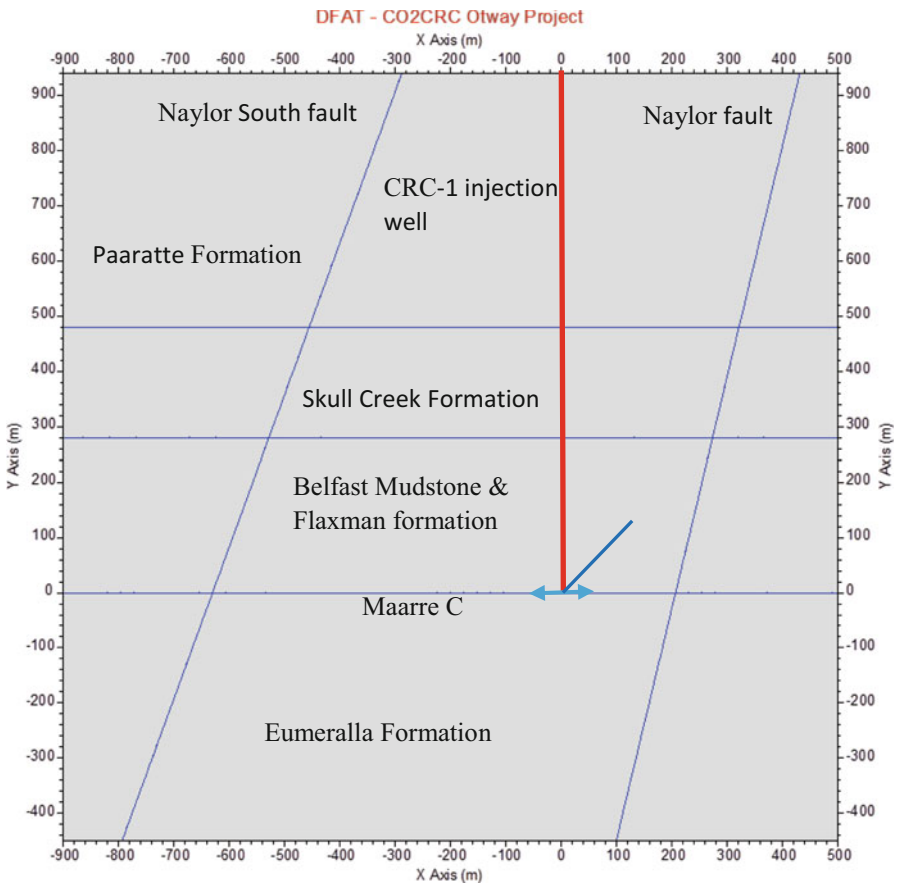


Fig. 11.16 Numerical model with an inclined joint in cap-rock. The joint dip angle varies from 45° to 90°

Table 11.3 Summary of modelling results on joint stability

Injection pressure (MPa)	Joint dip angle = 45°	Joint dip angle = 60°	Joint dip angle = 90°
19.2	<u>Joint shearing:</u> NIL <u>Joint opening:</u> NIL <u>Joint propagation:</u> NIL	<u>Joint shearing:</u> NIL <u>Joint opening:</u> NIL <u>Joint propagation:</u> NIL	<u>Joint shearing:</u> NIL <u>Joint opening:</u> NIL <u>Joint propagation:</u> NIL
25	<u>Joint shearing:</u> YES <u>Joint opening:</u> NIL <u>Joint propagation:</u> NIL	<u>Joint shearing:</u> YES <u>Joint opening:</u> NIL <u>Joint propagation:</u> NIL	<u>Joint shearing:</u> NIL <u>Joint opening:</u> NIL <u>Joint propagation:</u> NIL
30	<u>Joint shearing:</u> YES <u>Joint opening:</u> NIL <u>Joint propagation:</u> NIL	<u>Joint shearing:</u> YES <u>Joint opening:</u> NIL <u>Joint propagation:</u> NIL	<u>Joint shearing:</u> NIL <u>Joint opening:</u> YES <u>Joint propagation:</u> NIL

a length of 144 m and its strength parameters are assumed to be the same as those for the Naylor and Naylor South faults. The joint mechanical properties are assumed to be: normal stiffness $K_n = 100$ GPa/m; shear stiffness $K_s = 100$ GPa/m; friction angle = 30°; dilation angle = 0°; cohesion = 0 MPa; mode I fracture toughness $K_{IC} = 1.5$ MPa m^{0.5}; mode II fracture toughness $K_{IIC} = 3.0$ MPa m^{0.5}. The possibility of shearing and propagation of this joint has been studied with different injection pressures.

Results are shown in Table 11.3. With an injection pressure of 19.2 MPa, no shear or opening failure is predicted for the joint regardless of its dip angle. If the injection pressure is 25 MPa or higher, when the joint dip angle is 45° or 60°, the joint is predicted to experience shear failure, but no opening in tension or propagation. When the joint is vertical, no shear failure is expected because of the lack of shear stress in the joint plane for the values of injection pressure. At injection pressure of 25 MPa, the vertical joint is predicted to remain closed. When the injection pressure is increased to 30 MPa, which is close to the minimum principal horizontal stress at the Waarre C reservoir, the joint is predicted to open up, but not propagate.

We have also investigated the possibility of cap-rock failure in another situation where the rock contains a set of very weak bedding planes. In sedimentary rocks such as that at the Otway Project site, bedding planes are fairly common. In most cases, the bedding planes are horizontal or sub-horizontal. At the Otway project site, sub-horizontal bedding planes in the cap-rock are unlikely to fail because they align with the principal stress directions and very limited shear stress exists along the bedding planes. The CO₂ injection in Waarre C reservoir will not significantly change the stress magnitude as discussed previously. For this reason, we do not expect any failure on the bedding plane for an injection pressure up to 30 MPa.

However, in some special cases where the bedding planes are extremely weak and are inclined (say, 45°), there is a possibility of fracturing along the bedding planes. To investigate this possibility, a number of cases with different bedding plane strength and bedding angle have been investigated. It was found that with a bedding plane angle of 45°, fracture initiation could occur in the cap-rock if the bedding plane

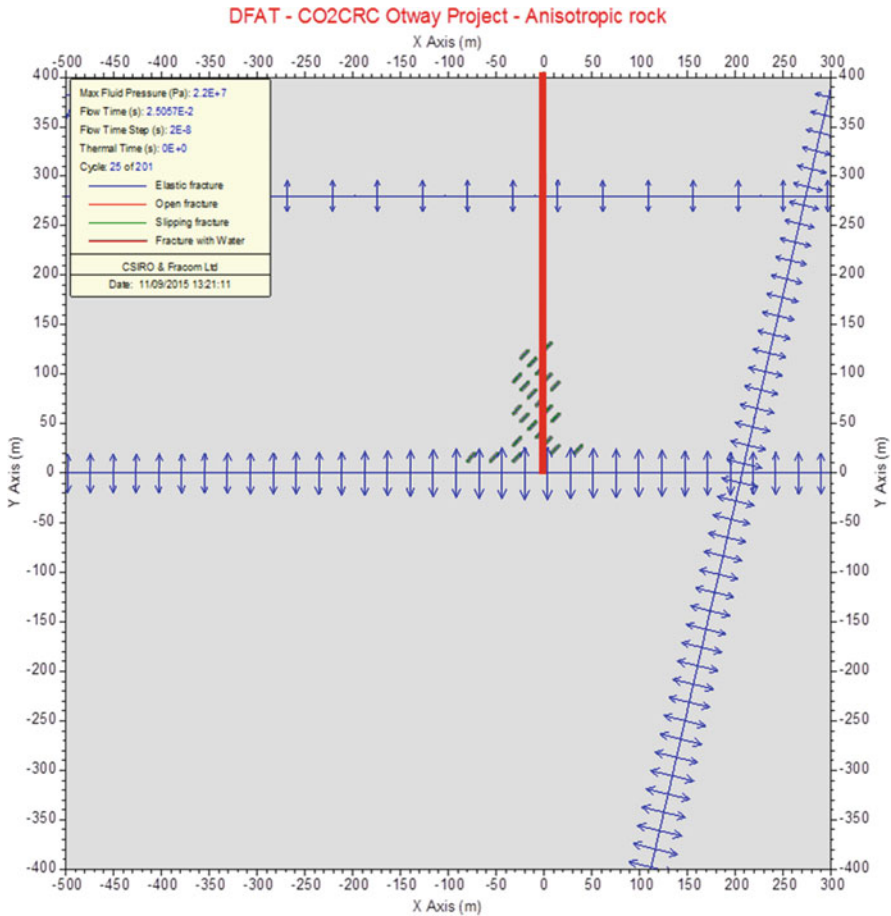


Fig. 11.17 Predicted fracture initiation along weak bedding planes. Bedding plane friction angle is 11° , cohesion = 0; bedding angle $=45^\circ$. Injection pressure = 25 MPa, initial pore pressure = 16 MPa

has a friction angle of 11° or less and no cohesion. New fractures are formed in the vicinity of the injection well in the cap-rock. These fractures are all formed along the bedding plane direction, see Fig. 11.17.

Figure 11.17 is a special case where the bedding planes are in a critical balanced state before injection. The small stress increase (0.37 MPa with injection pressure of 25 MPa) in the immediate cap-rock disturbs this subtle balance and causes cap-rock fracturing. This case is considered to be extremely rare and should not be taken as a likely scenario at Otway Project site.

11.4 Conclusions

Rock fracturing may occur in the vicinity of an underground opening due to the elevation of tangential stress and removal of the confining stress. Shallow spalling in the tunnel periphery (arch or wall) is believed to be caused by tensile fracturing from extensional strain, although no tensile stress exists there. Massive scale failure however is most likely to be caused by shear fracturing under high compressive stresses.

Rock fracturing and failure can be limited when one or more joint sets are present, due to shear-stress dissipation on the joints, as opposed to the need for more stress-dissipating fracturing of intact rock, in order to gain equilibrium. So *lack of jointing* could be a source of risk in deep hard-rock tunnels, whereas the presence of jointing can sometimes be a source of risk in shallow tunnels. The same principles apply to mining in hard, strong coal seams overlain by a massive sandstone unit, where energy release from fracturing cannot be adequately absorbed and hence large scale failure can be triggered.

The hydraulic-fracturing coupled model of FRACOD is applied to simulate a CO₂ geo-sequestration project site in Australia with simplified geology. Existing faults re-activation and cap-rock stabilities have been studied in detail. Modelling predicts that the site is stable under the real injection conditions and this agrees with other simulations and the site monitoring.

References

- Aruffo CM, Rodriguez-Herrera A, Tenthorey E, Krzikalla F, Minton J, Henk A (2014) Geomechanical modelling to assess fault integrity at the CO₂CRC Otway Project, Australia. *Aust J Earth Sci* 61:987–1001. <https://doi.org/10.1080/08120099.2014.958876>
- Barton N, Grimstad E (2014) Q-system – an illustrated guide following forty years in tunnelling. 44p. 79 figs, photos: web-site: www.nickbarton.com
- Barton N, Shen B (2017) Risk of shear failure and extensional failure around over-stressed excavations in brittle rock. *J Rock Mech Geotech Eng* 9(2):210–225
- Cai M, Kaiser PK (2014) In-situ rock spalling strength near excavation boundaries. *Rock Mech Rock Eng* 47:659–675
- Cook PJ (2014) Geologically storing carbon – learning from the Otway project experience. CSIRO Publishing, Melbourne. ISBN 9781484302307
- Daniel RF (2007) Carbon dioxide seal capacity study. CRC-1, CO₂CRC Otway Project, Otway Basin, Victoria. CO₂CRC Report No: RPT07-0629
- Dresen G, Stanchits S, Rybacki E (2010) Borehole breakout evolution through acoustic emission location analysis. *Int J Rock Mech Min Sci* 47:426–435
- Fairhurst C, Cook NGW (1967) The phenomenon of rock splitting parallel to the direction of maximum compression in the neighbourhood of a surface. *Proceedings of the 1st Congress ISRM, Lisbon, vol 1, pp 687–692*

- Grimstad E, Barton N (1993) Updating the Q-system for NMT. In: Proceedings of international symposium on sprayed concrete-modern use of wet mix sprayed concrete for underground support. Norwegian Concrete Association, Oslo, pp 1–20
- Hoek E, Brown ET (1980) Underground excavations in rock. Institution of Mining and Metallurgy, London. 527p
- Islam MA, Skalle P (2013) An experimental investigation of shale mechanical properties through drained and undrained test mechanisms. *Rock Mech Rock Eng* 46(6):1391–1413. <https://doi.org/10.1007/s00603-013-0377-8>
- Jing L (2003) A review of techniques, advances and outstanding issues in numerical modelling for rock mechanics and rock engineering. *Int J Rock Mech Min Sci* 40:283–353
- Martin CD (1997) The effect of cohesion loss and stress path on brittle rock strength. Seventeenth Canadian Geotechnical Colloquium. *Can Geotech J* 34:698–725
- Martin CD, Kaiser PK, McCreath DR (1999) Hoek–Brown parameters for predicting the depth of brittle failure around tunnels. *Can Geotech J* 36:136–151
- NSW Mine Safety Investigation Unit (2015) Report into the deaths of James Mitchell and Phillip Grant at the Austar Coal Mine, Paxton, NSW on 15 April 2014. Report prepared by the NSW Mine Safety Investigation Unit
- Shen B, Barton N (2018) Rock fracturing mechanisms around underground openings. *Geomech Eng* 16(1):35–47. <https://doi.org/10.12989/gae.2018.16.1035>
- Shen B, Shi J (2016) Analysis of fracturing-hydraulic coupling in transversely isotropic rocks and a case study on CO₂ sequestration. *Int J Rock Mech Min Sci* 88:206–220
- Shen B, Stephansson O, Rinne M (2014) Modelling rock fracturing processes: a fracture mechanics approach using FRACOD. Springer (publisher), Dordrecht. 173p, ISBN 978-94-007-6903
- Siren T (2012) Fracture toughness properties of rocks in Olkiluoto: laboratory measurements 2008–2009, Posiva Report. Posiva, Olkiluoto, pp 2012–2025
- Stacey TR (1981) A simple extension strain criterion for fracture of brittle rock. *Int J Rock Mech Min Sci Geomech Abstr* 18:469–474
- Vidal-Gilbert S, Tenthorey E, Dewhurst D, Ennis-King J, Ruth PV, Hillis R (2010) Geomechanical analysis of the Naylor Field, Otway Basin, Australia: implications for CO₂ injection and storage. *Int J Greenhouse Gas Control* 4:827–839
- Wesseloo J, Stacey TR (2016) A reconsideration of the extension strain criterion for fracture and failure of rock. *Rock Mech Rock Eng* 49:4667–4679